
This copy is for your personal, non-commercial use only.

If you wish to distribute this article to others, you can order high-quality copies for your colleagues, clients, or customers by [clicking here](#).

Permission to republish or repurpose articles or portions of articles can be obtained by following the guidelines [here](#).

The following resources related to this article are available online at www.sciencemag.org (this information is current as of August 25, 2014):

Updated information and services, including high-resolution figures, can be found in the online version of this article at:

<http://www.sciencemag.org/content/345/6197/660.full.html>

Supporting Online Material can be found at:

<http://www.sciencemag.org/content/suppl/2014/08/06/345.6197.660.DC1.html>

This article **cites 48 articles**, 10 of which can be accessed free:

<http://www.sciencemag.org/content/345/6197/660.full.html#ref-list-1>

This article appears in the following **subject collections**:

Neuroscience

<http://www.sciencemag.org/cgi/collection/neuroscience>

and the bosonic field, v is the quartic coupling among the bosonic fields, λ is the linear coupling between the bosonic field and the orthorhombic lattice distortion ϵ , and \mathbf{q} is the momentum transfer within one Brillouin zone. Minimizing the action with respect to ϵ , we arrive at $\epsilon = \lambda \langle \Delta \rangle / C_s$, where C_s is the shear modulus. In other words, the orthorhombic lattice distortion is proportional to the nematic order parameter $\langle \Delta \rangle$, and both are expected to develop nonzero expectation values below T_s (12–14). However, the nematic field Δ undergoes fluctuations in the tetragonal phase above T_s while lattice distortion ϵ remains zero. These fluctuations will be observable in dynamic quantities, such as the finite-energy spin fluctuations, and in transport measurements. We therefore conclude that the scale T^* , below which we observe anisotropy of low-energy spin fluctuations (Figs. 3E, 4E, and 4F) and where the resistivity anisotropy is observed (Fig. 3E, right inset), marks a typical range of the nematic fluctuations.

Several remarks are in order. First, the applied uniaxial pressure used to detwin the samples will induce a finite value of ϵ at any temperature, so that strictly speaking, the structural transition at T_s will be rendered a crossover. In practice, however, the applied pressure is too small to cause a perceptible lattice distortion, which is why the transition temperature T_s as determined from the extinction effect of the nuclear (2, -2, 0) Bragg peak remains unchanged from the zero-pressure case [fig. S2, B and D] (26, 27). On the other hand, the extent of nematic fluctuations may be sensitive to the shear strain, in agreement with the reported increase of T^* (as determined from resistivity anisotropy) with the uniaxial pressure (37). Second, in Eq. 1 the variable Δ could equally signify the orbital order $\Delta \propto (n_{xz} - n_{yz})$ which lifts the degeneracy between the Fe d_{xz} and d_{yz} orbitals. In fact, the two order parameters will couple linearly to each other, $(\mathbf{M}_1 \cdot \mathbf{M}_2) \propto (n_{xz} - n_{yz})$, so that both will develop a nonzero value below T_s . In this respect, our findings are also consistent with the recent ARPES finding of an orbital ordering (17, 18) in BaFe_2As_2 . This underlines the complementarity of the spin-nematic and orbital descriptions of the C_4 symmetry breaking. Third, in the nearly optimally electron-doped superconductor, we observe anisotropy of the low-lying spin excitations in the tetragonal phase $T_s < T < T^*$, even though the orbital order is no longer detectable by ARPES (17, 18). This is consistent with the absence of a static nematic order $\langle \Delta \rangle = 0$ above T_s , whereas the observed spin anisotropy originates from Ising-nematic fluctuations. Because T_s is considerably suppressed for this doping, these fluctuations are quantum rather than thermal: They persist beyond the immediate vicinity of T_s , and the associated spin anisotropy should have sizable dependence on frequency that can be probed by future experiments. Fourth, when resistivity anisotropy under uniaxial strain disappears in the electron-overdoped sample (10), the uniaxial-strain-induced spin excitation anisotropy also vanishes (Fig. 1E and fig. S5), which suggests a direct connection between these two phenomena.

Finally, our measurements in the spin channel do not necessarily signal a thermodynamic order at the temperature T^* . Rather, T^* likely signals a crossover, whereas the true nematic transition occurs at T_s (9). This implies that a static order above T_s inferred from recent measurements of magnetic torque anisotropy in the isoalant $\text{BaFe}_2\text{As}_{2-x}\text{P}_x$ (38) is most likely not in the spin channel accessible to the inelastic neutron scattering. A static order in other channels—such as, for instance, an octupolar order—would, however, not contradict our observations.

REFERENCES AND NOTES

- Y. Kamihara, T. Watanabe, M. Hirano, H. Hosono, *J. Am. Chem. Soc.* **130**, 3296–3297 (2008).
- G. R. Stewart, *Rev. Mod. Phys.* **83**, 1589–1652 (2011).
- P. C. Dai, J. Hu, E. Dagotto, *Nat. Phys.* **8**, 709–718 (2012).
- C. de la Cruz, Q. Huang, J. W. Lynn, J. Li, W. Ratcliff II, J. L. Zarestky et al., *Nature* **453**, 899–902 (2008).
- Q. Huang et al., *Phys. Rev. Lett.* **101**, 257003 (2008).
- M. G. Kim et al., *Phys. Rev. B* **83**, 134522 (2011).
- J. H. Chu et al., *Science* **329**, 824–826 (2010).
- M. A. Tanatar et al., *Phys. Rev. B* **81**, 184508 (2010).
- J. H. Chu, H.-H. Kuo, J. G. Analytis, I. R. Fisher, *Science* **337**, 710–712 (2012).
- I. R. Fisher, L. Degiorgi, Z. X. Shen, *Rep. Prog. Phys.* **74**, 124506 (2011).
- E. Fradkin, S. A. Kivelson, M. J. Lawler, J. P. Eisenstein, A. P. Mackenzie, *Annu. Rev. Condens. Matter Phys.* **1**, 153–178 (2010).
- R. M. Fernandes, A. V. Chubukov, J. Schmalian, *Nat. Phys.* **10**, 97–104 (2014).
- C. Fang, H. Yao, W.-F. Tsai, J. P. Hu, S. A. Kivelson, *Phys. Rev. B* **77**, 224509 (2008).
- J. Dai, Q. Si, J. X. Zhu, E. Abrahams, *Proc. Natl. Acad. Sci. U.S.A.* **106**, 4118–4121 (2009).
- M. P. Allan et al., *Nat. Phys.* **9**, 220–224 (2013).
- S. Ishida et al., *Phys. Rev. Lett.* **110**, 207001 (2013).
- M. Yi et al., *Proc. Natl. Acad. Sci. U.S.A.* **108**, 6878–6883 (2011).
- Y. Zhang et al., *Phys. Rev. B* **85**, 085121 (2012).
- C. C. Lee, W. G. Yin, W. Ku, *Phys. Rev. Lett.* **103**, 267001 (2009).
- F. Krüger, S. Kumar, J. Zaanen, J. van den Brink, *Phys. Rev. B* **79**, 054504 (2009).

- W. C. Lv, J. S. Wu, P. Phillips, *Phys. Rev. B* **80**, 224506 (2009).
- C.-C. Chen et al., *Phys. Rev. B* **82**, 100504 (2010).
- H. Luo et al., *Phys. Rev. Lett.* **108**, 247002 (2012).
- X. Lu et al., *Phys. Rev. Lett.* **110**, 257001 (2013).
- C. Dhital et al., *Phys. Rev. Lett.* **108**, 087001 (2012).
- Yu. Song et al., *Phys. Rev. B* **87**, 184511 (2013).
- Materials and methods are available as supplementary materials on Science Online.
- C. Lester et al., *Phys. Rev. B* **79**, 144523 (2009).
- A. Kreyssig et al., *Phys. Rev. B* **81**, 134512 (2010).
- J. T. Park et al., *Phys. Rev. B* **86**, 024437 (2012).
- L. W. Harriger et al., *Phys. Rev. B* **84**, 054544 (2011).
- M. Nakajima et al., *Phys. Rev. Lett.* **109**, 217003 (2012).
- M. Y. Wang et al., *Phys. Rev. B* **83**, 094516 (2011).
- P. Chandra, P. Coleman, A. I. Larkin, *Phys. Rev. Lett.* **64**, 88–91 (1990).
- R. M. Fernandes, J. Schmalian, *Supercond. Sci. Technol.* **25**, 084005 (2012).
- The Ginzburg-Landau action up to the 4th power of $\mathbf{M}_{1/2}$: $S_0[\mathbf{M}_1^2, \mathbf{M}_2^2] = \int [d\mathbf{q} d\omega] (r_0 + \mathbf{q}^2 + \gamma|\omega|) (\mathbf{M}_1^2 + \mathbf{M}_2^2) + u(\mathbf{M}_1^2 + \mathbf{M}_2^2)^2$, where $r_0 \propto T - T_N$ describes distance from the Néel point.
- H.-H. Kuo et al., *Phys. Rev. B* **84**, 054540 (2011).
- S. Kasahara et al., *Nature* **486**, 382–385 (2012).

ACKNOWLEDGMENTS

The work at the Institute of Physics, Chinese Academy of Sciences is supported by Ministry of Science and Technology of China (973 project: 2012CB821400 and 2011CBA00110), National Natural Science Foundation of China and China Academy of Engineering Physics. The work at Rice is supported by the U.S. NSF-DMR-1308603 and DMR-1362219 (P.D.), by Robert A. Welch Foundation grant no. C-1839 (P.D.), P-1818 (A.H.N.), and no. C-1411 (Q.S.), and by the U.S. NSF-DMR-1309531 and the Alexander von Humboldt Foundation (Q.S.). A.H.N. and Q.S. acknowledge the hospitality of the Aspen Center for Physics, where support was provided by NSF grant PHYS-1066293.

SUPPLEMENTARY MATERIALS

www.sciencemag.org/content/345/6197/657/suppl/DC1
Materials and Methods
Figs. S1 to S5
References (39, 40)

6 February 2014; accepted 25 June 2014
Published online 31 July 2014;
10.1126/science.1251853

SELECTIVE ATTENTION

Long-range and local circuits for top-down modulation of visual cortex processing

Siyu Zhang,¹ Min Xu,¹ Tsukasa Kamigaki,¹ Johnny Phong Hoang Do,¹ Wei-Cheng Chang,¹ Sean Jenvay,¹ Kazunari Miyamichi,^{2*} Liqun Luo,² Yang Dan^{1†}

Top-down modulation of sensory processing allows the animal to select inputs most relevant to current tasks. We found that the cingulate (Cg) region of the mouse frontal cortex powerfully influences sensory processing in the primary visual cortex (V1) through long-range projections that activate local γ -aminobutyric acid-ergic (GABAergic) circuits. Optogenetic activation of Cg neurons enhanced V1 neuron responses and improved visual discrimination. Focal activation of Cg axons in V1 caused a response increase at the activation site but a decrease at nearby locations (center-surround modulation). Whereas somatostatin-positive GABAergic interneurons contributed preferentially to surround suppression, vasoactive intestinal peptide-positive interneurons were crucial for center facilitation. Long-range corticocortical projections thus act through local microcircuits to exert spatially specific top-down modulation of sensory processing.

Sensory processing is strongly modulated by the animal's behavioral state. A well-known example is top-down attention, a powerful mechanism for selective processing of behaviorally relevant information

and filtering out irrelevant stimuli. In visual cortical areas, many neurons exhibit enhanced responses to attended stimuli (1–4). Several frontal and parietal cortical regions have been implicated as the sources of top-down modulation

signals (1, 2, 5, 6), especially the dorsolateral prefrontal cortex and frontal eye field (FEF) (7–13). Electrical stimulation of the FEF enhanced V4 neuron responses at the retinotopically corresponding location and suppressed responses at other locations (11), resembling the center-surround profile of attentional modulation (1, 3, 14, 15). Beyond identifying the signal sources, however, the synaptic circuits mediating top-down modulation are largely unknown. In addition to corticocortical projections, FEF also projects to the thalamus and other subcortical circuits that modulate cortical processing (16–20). The role of each pathway has not been clearly delineated. Furthermore, because long-range corticocortical projections are primarily glutamatergic, whether and how they provide center-surround modulation is unknown.

To examine the circuit mechanism of top-down modulation in mouse brain, we first identified neurons in the frontal cortex that directly project to visual cortex by injecting fluorescent latex mi-

crospores (Retrobeads) into V1. We found numerous retrogradely labeled neurons in the cingulate (Cg) area (Fig. 1, A to C; and fig. S1, A and B). To visualize the axonal projections from Cg excitatory neurons, we injected adeno-associated virus [AAV-CaMKII α -hChR2(H134R)-EYFP] into Cg. We found enhanced yellow fluorescent protein (EYFP)-labeled axons in both V1 and surrounding visual areas, with the axons in V1 preferentially distributed in layers 1 and 6 (Fig. 1E and fig. S1C). Cg neurons also project to the superior colliculus (Fig. 1, D and E) (21).

To test the functional influence of Cg neuron activity on visual processing, we applied laser stimulation to the Cg of the mouse injected with AAV-CaMKII α -hChR2(H134R)-EYFP (Fig. 2A), which evoked reliable neuronal spiking (Fig. 2B). Cell-attached recordings in V1 of anesthetized mice measured neuronal responses to drifting grating stimuli in both control (laser-off) and Cg activation (laser-on) trials. Cg activation strongly increased V1 neuron firing rate at the preferred orientation but not at nonpreferred orientation (Fig. 2C). This resulted in an approximately multiplicative scaling of the tuning curve (Fig. 2, C and D), similar to the effects of top-down attention (22) and FEF stimulation (17). Cg activation also increased the slope of V1 neuron response as a function of stimulus contrast (contrast-response function) (fig. S2B). In control mice not injected

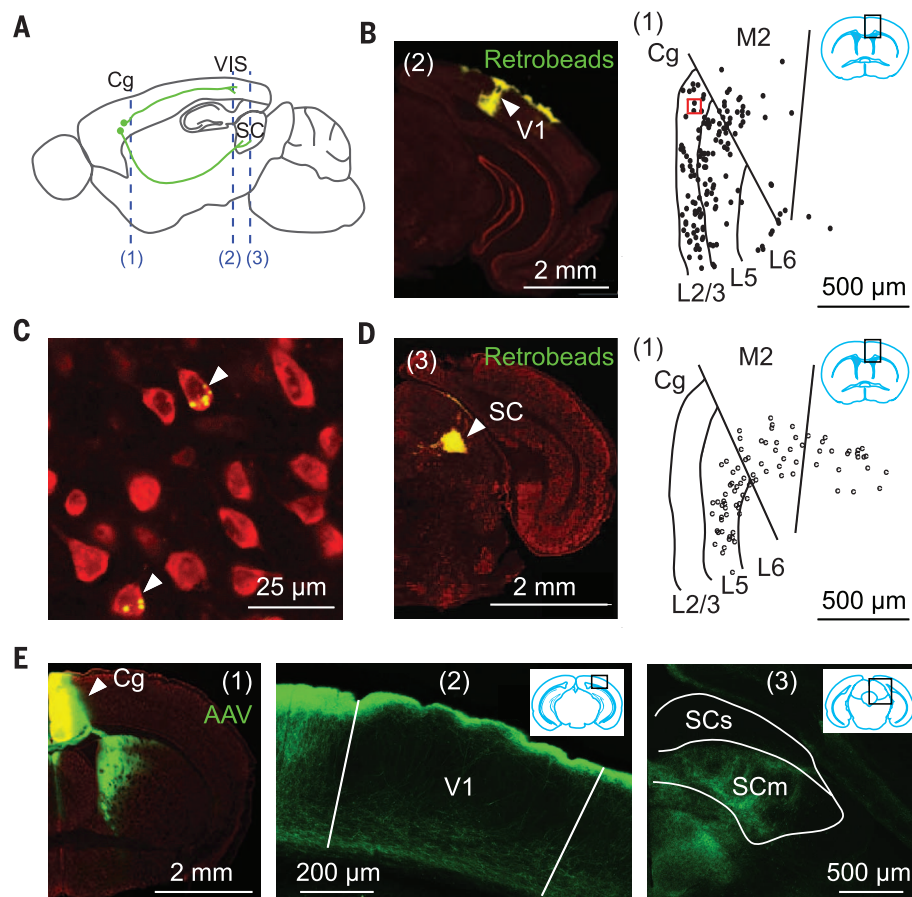
with AAV, laser stimulation had no effect (fig. S2, C and D), and the laser-induced response increase was significantly higher in the ChR2 than control mice ($P = 8 \times 10^{-4}$, t test).

To further test the functional influence of Cg activity, we applied optogenetic manipulations in awake mice. Cg activation enhanced V1 responses at a level comparable with that in anesthetized mice (Fig. 2, D and E). Conversely, inactivation of Cg excitatory neurons significantly decreased V1 responses. Stimulation of primate FEF not only enhances visual cortical responses but also improves perceptual performance (23). We thus tested the behavioral effect of Cg activation in mice trained to perform a visual discrimination task. Cg activation significantly improved the performance ($P < 0.02$ for each of 5 mice, paired t test) (Fig. 2F). In control mice injected with AAV-CaMKII α -mCherry, laser had no effect ($P > 0.42$), and the laser-induced improvement was significantly greater for the ChR2 than control mice ($P = 8 \times 10^{-4}$, t test). The laser stimulation used in these experiments evoked no notable eye movement, although stimulation at much higher laser power and frequencies could evoke saccade-like movement.

In principle, Cg neuron activity can influence V1 processing through either the direct projection or indirect pathways via other brain structures. To test whether the direct projection is sufficient for the modulation, we optogenetically

¹Division of Neurobiology, Department of Molecular and Cell Biology, Helen Wills Neuroscience Institute, Howard Hughes Medical Institute, University of California, Berkeley, CA 94720, USA. ²Department of Biology, Howard Hughes Medical Institute, Stanford University, Stanford, CA 94305, USA. *Present address: Department of Applied Biological Chemistry, Graduate School of Agricultural and Life Sciences, The University of Tokyo, Tokyo 113-8657, Japan. †Corresponding author. E-mail: ydan@berkeley.edu

Fig. 1. Cg projects to visual cortex and superior colliculus (SC). (A) Schematic of Cg projections. Dashed lines indicate locations of coronal sections shown in this figure: (1), Cg; (2), V1; (3), SC. (B to D) Retrograde tracing. (B) (Left) Fluorescence image at location (2) showing retrobeads (green) injected into V1. Arrowhead, injection site; red, Nissl staining. (Right) Labeled neurons (dots) at (1), in region outlined by black rectangle (inset). (C) Fluorescence image for red square in (B). Arrowheads indicate labeled neurons. (D) Similar to (B), with retrobeads injected into SC. (E) Anterograde tracing from Cg. (Left) Fluorescence image at (1). Arrowhead indicates AAV injection site. (Middle and right) Cg projections to V1 and SC, respectively. SCs/SCm, sensory/motor-related SC.



activated Cg axons in V1 of anesthetized mice (Fig. 3A). Laser stimulation in a small area (~200 μm in diameter) encompassing the recorded cell (Fig. 3B) increased both the tuning curve amplitude (Fig. 3, C and D, left) and contrast-response slope (fig. S3). The magnitude of increase was ~70% of that induced through Cg neuron activation (Fig. 2, D and E).

In primates, both top-down attention and FEF stimulation exert center-surround modulation of visual cortical responses (1, 3, 11, 14, 15). We next systematically varied the location of laser stimulation relative to the recorded cell (Fig. 3B). Laser

stimulation at 200 μm significantly decreased the tuning curve amplitude (Fig. 3, C and D, right). The spatial profile of response modulation consisted of a facilitatory center and a suppressive surround (Fig. 3E), reminiscent of the effects of top-down attention (1, 3, 14, 15) and FEF stimulation (11). Activation of Cg axons could antidromically induce spiking of the cell bodies, which may activate axon collaterals to other brain areas. We thus repeated the axon stimulation experiment after blocking spiking in Cg with 2% lidocaine. Similar center-surround modulation was still observed in V1 (fig. S4).

Because the Cg→V1 projections activated in our experiments are glutamatergic, the center-surround modulation is likely to involve V1 local circuits. We therefore made whole-cell recordings in V1 slices. Because the topical laser stimulation used in vivo (Fig. 3, A and B) is likely to activate Cg axons in layer 1 preferentially, in slice experiments we also stimulated layer 1 axons (fig. S5A). We found both excitatory and inhibitory postsynaptic currents (EPSCs and IPSCs) in layer 2/3 pyramidal neurons near the laser stimulation site (fig. S5B). The EPSCs showed short-onset latencies (1.9 ± 0.1 ms, mean \pm SEM),

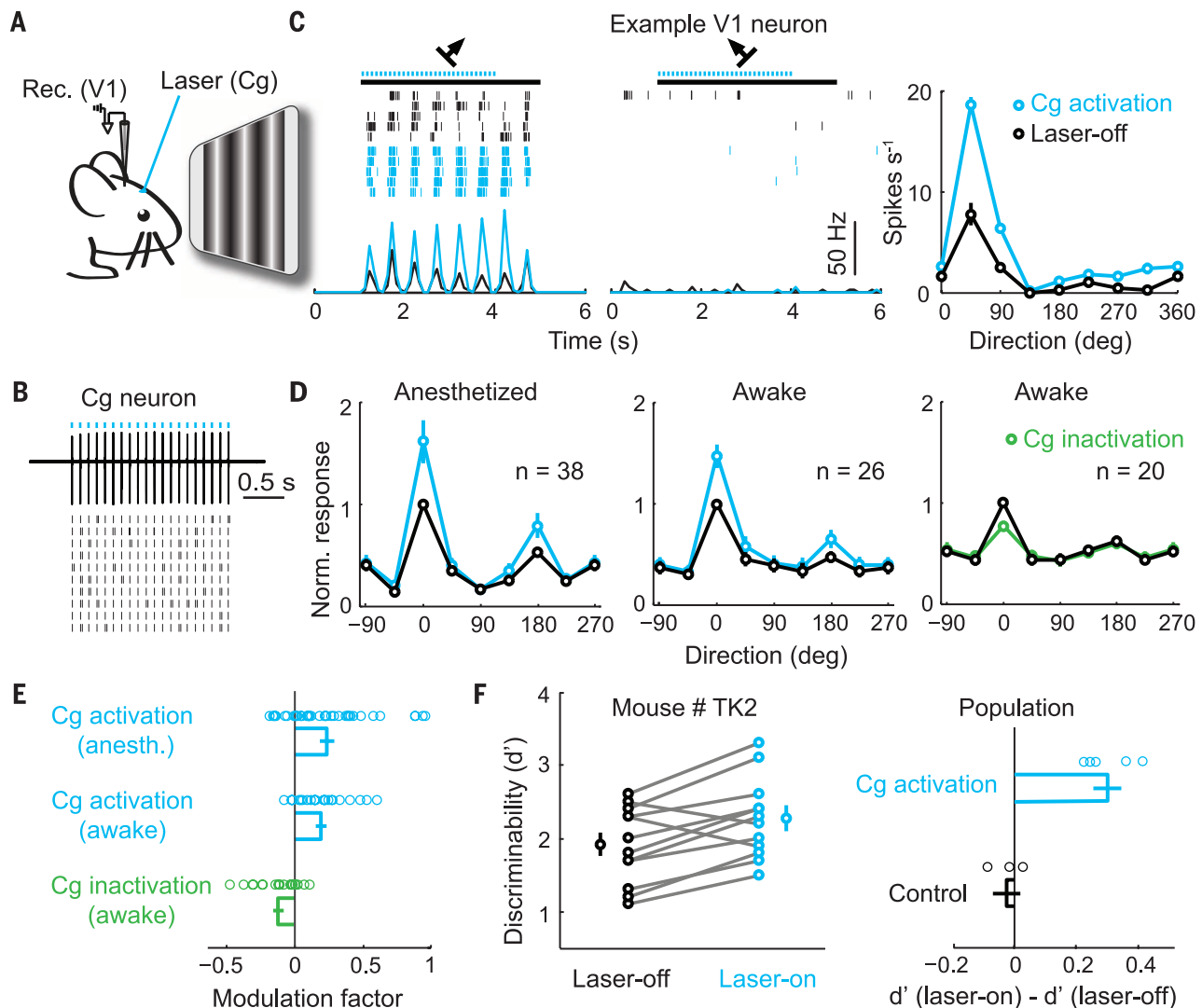


Fig. 2. Cg activation enhances V1 neuron responses and improves visual discrimination. (A) Schematic of experiment. (B) Cg neuron spiking induced by laser (5 ms/pulse, 10 Hz, blue dots). (Top) Example trace. (Bottom) Raster plot. (C) Visual response of a V1 neuron with (blue) or without (black) Cg activation. (Left and middle) Raster plots and PSTHs at preferred and nonpreferred orientations, respectively. Black bar indicates duration of visual stimulation (4 s). (Right) Orientation tuning of this neuron. Error bar, \pm SEM. (D) Population average of orientation tuning, with each neuron normalized and aligned by its optimal orientation without laser. (Left and middle) Tuning with (blue) and without (black) Cg activation in anesthetized and awake mice, respectively. (Right) Tuning with (green) and without (black) Cg inactivation in awake mice. (E) Modulation factors. Cg activation, anesthetized, $0.24 \pm$

0.05 (mean \pm SEM), $P = 10^{-4}$ (t test), $n = 38$ neurons; awake, 0.19 ± 0.04 , $P = 6 \times 10^{-5}$, $n = 26$ neurons; Cg inactivation: awake, -0.12 ± 0.03 , $P = 0.003$, $n = 20$ neurons. Each circle represents one neuron. (F) Effect of Cg activation on visual discrimination performance. (Left) An example mouse. Each pair of circles represent d' measured in one day ($n = 11$ days). Laser-on (blue), 2.27 ± 0.16 (mean \pm SEM); laser-off (black), 1.91 ± 0.16 , $P = 0.005$, paired t test. (Right) Population summary of laser-induced change in d' , for Cg activation [mice injected with AAV2/2-CaMKII α -hChR2(H134R)-EYFP, 0.30 ± 0.04 , $n = 5$ mice] and control (AAV2/2-CaMKII α -mCherry, -0.02 ± 0.04 , $n = 3$ mice) groups. $P_{\text{laser}} = 0.002$, $P_{\text{group}} = 0.59$, $P_{\text{interaction}} = 0.0009$ [two-way mixed analysis of variance]; laser had significant effect only in ChR2 group ($P = 0.0006$, post-hoc Tukey's test).

suggesting monosynaptic inputs from Cg axons. However, the IPSCs showed significantly longer latencies (6.2 ± 0.4 ms, $P = 5 \times 10^{-14}$, paired t test) and were completely blocked by 6-cyano-7-nitroquinoxaline-2,3-dione (CNQX; 10 μ M) (fig. S5C), suggesting disynaptic inhibition. We then measured the excitatory and inhibitory inputs as functions of distance between laser stimulation and the recorded cell (fig. S5, D and E). Although the strength of excitatory input decreased monotonically, the inhibitory input was stronger at 200 μ m than at 0 μ m. Such a spatial profile seems well suited for generating surround suppression in vivo (Fig. 3E).

The Cg axon-induced disynaptic inhibition of pyramidal neurons should originate from local γ -aminobutyric acid-ergic (GABAergic) neurons. Parvalbumin-positive (PV+), somatostatin-positive (SOM+), and vasoactive intestinal peptide-positive (VIP+) interneurons are three major nonoverlapping populations of cortical GABAergic neurons (24, 25) and play different roles in visual processing (26–28). To assess the role of each subtype in top-down modulation, we first measured their responses to Cg axon stimulation. Each subtype was identified by breeding loxP-flanked tdTomato reporter mice with PV-, SOM-, or VIP-Cre mice (fig. S6A). Activation of layer 1 Cg axons evoked short-latency (~ 3 ms) excitatory postsynaptic potentials (EPSPs) in all three

interneuron subtypes, even after V1 neuron spiking was blocked with tetrodotoxin (TTX) (fig. S6, B to G) (29). Rabies virus-mediated monosynaptic retrograde tracing (30) confirmed that all three subtypes received direct Cg innervation (fig. S7). The Cg input was stronger in VIP+ than the other neuron types in layer 2/3 (fig. S6), similar to the motor→somatosensory cortex input (31).

We next measured the contribution of each interneuron subtype to disynaptic inhibition of pyramidal neurons using optogenetic inactivation. To express halorhodopsin (Halo) in each subtype, we crossed PV-, SOM-, or VIP-Cre mice with loxP-flanked Halo reporter mice (32). ChR2 was expressed in Cg excitatory neurons by using AAV-CaMKII α -hChR2(H134R)-EYFP. Inactivation of PV+ neurons (yellow laser, in an area >600 μ m in diameter) (Fig. 4A) reduced Cg axon-induced inhibitory inputs at 0, 200, and 400 μ m, but the strongest inhibition was still observed at 200 μ m (Fig. 4B, left). In contrast, inactivating SOM+ neurons caused the largest reduction of inhibition at 200 μ m, so that the strength of inhibition decreased monotonically with distance (middle). Inactivating VIP+ neurons caused an increase in inhibition at 0 μ m and no change at other locations (right). Thus, VIP+ neurons caused spatially localized disinhibition, likely by preferentially innervating SOM+ neurons (31, 33–35).

Last, to test the roles of these interneuron subtypes in top-down modulation of visual processing, we optogenetically inactivated them while activating Cg axons in vivo (Fig. 4C). PV+ neuron inactivation caused similar response increases at 0, 200, and 400 μ m (Fig. 4, D and E, left). Their inactivation with yellow laser alone without Cg axon stimulation also induced a response increase ($P = 0.01$) (Fig. 4D, yellow circle), suggesting that the effect was partly due to a general reduction of cortical inhibition unrelated to Cg axon stimulation. SOM+ neuron inactivation caused the largest response increase at 200 μ m, converting the surround suppression into a slight facilitation (Fig. 4, D and E, middle). The increase at 200 μ m was greater than the effect of yellow laser alone ($P = 0.002$), indicating that SOM+ neurons contribute strongly to Cg axon-induced surround suppression. Inactivation of VIP+ neurons, on the other hand, blocked the center facilitation (at 0 μ m) without affecting surround suppression (Fig. 4, D and E, right).

We identified a region of mouse frontal cortex that can exert spatially specific top-down modulation of visual processing, which is a hallmark of selective attention. The spatial pattern of Cg projections (Fig. 1 and fig. S1) and its powerful modulation of visual processing indicate functional similarity between mouse Cg and primate

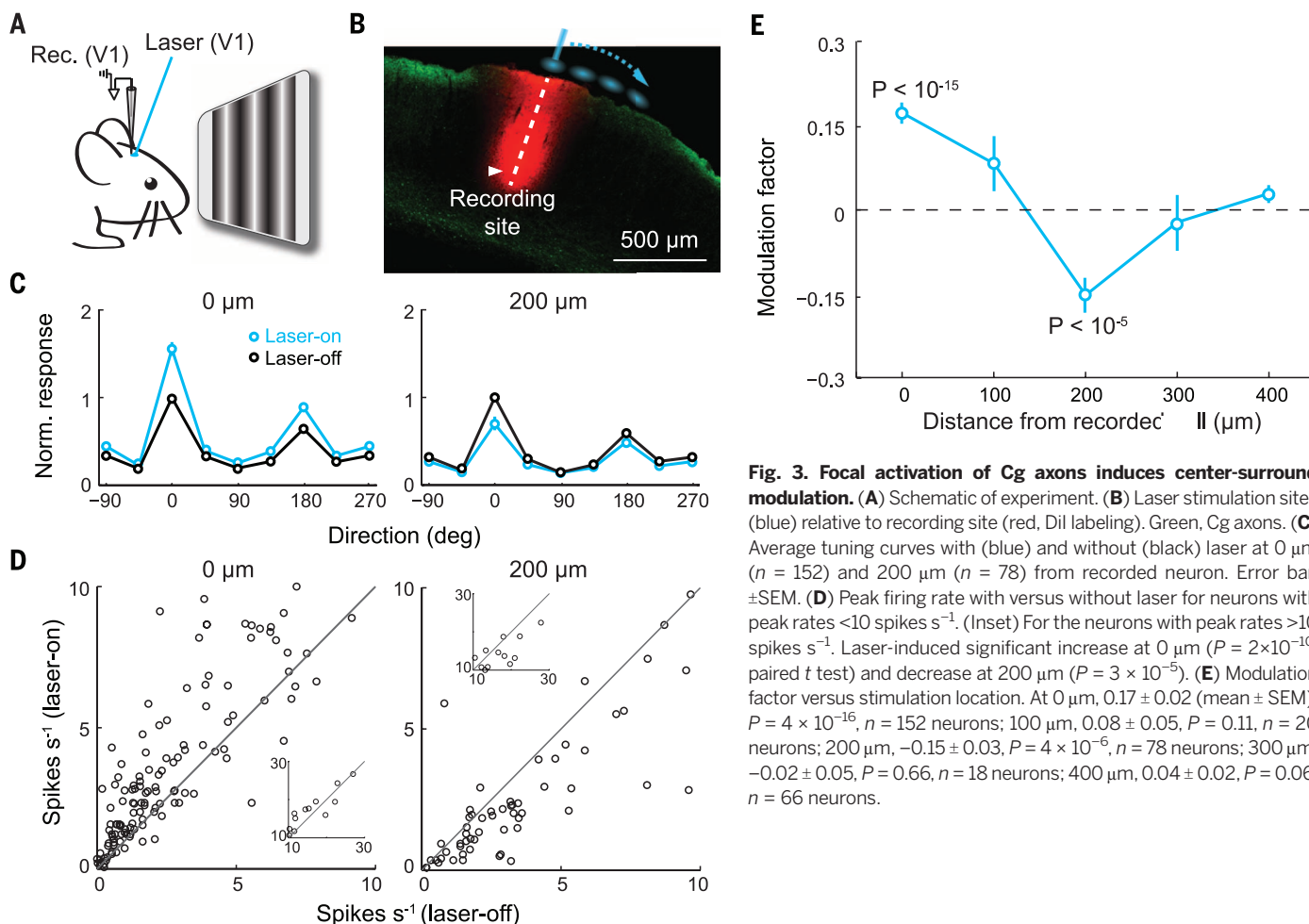


Fig. 3. Focal activation of Cg axons induces center-surround modulation. (A) Schematic of experiment. (B) Laser stimulation sites (blue) relative to recording site (red, Dil labeling). Green, Cg axons. (C) Average tuning curves with (blue) and without (black) laser at 0 μ m ($n = 152$) and 200 μ m ($n = 78$) from recorded neuron. Error bar, \pm SEM. (D) Peak firing rate with versus without laser for neurons with peak rates <10 spikes s^{-1} . (Inset) For the neurons with peak rates >10 spikes s^{-1} . Laser-induced significant increase at 0 μ m ($P = 2 \times 10^{-10}$, paired t test) and decrease at 200 μ m ($P = 3 \times 10^{-5}$). (E) Modulation factor versus stimulation location. At 0 μ m, 0.17 ± 0.02 (mean \pm SEM), $P = 4 \times 10^{-16}$, $n = 152$ neurons; 100 μ m, 0.08 ± 0.05 , $P = 0.11$, $n = 20$ neurons; 200 μ m, -0.15 ± 0.03 , $P = 4 \times 10^{-6}$, $n = 78$ neurons; 300 μ m, -0.02 ± 0.05 , $P = 0.66$, $n = 18$ neurons; 400 μ m, 0.04 ± 0.02 , $P = 0.06$, $n = 66$ neurons.

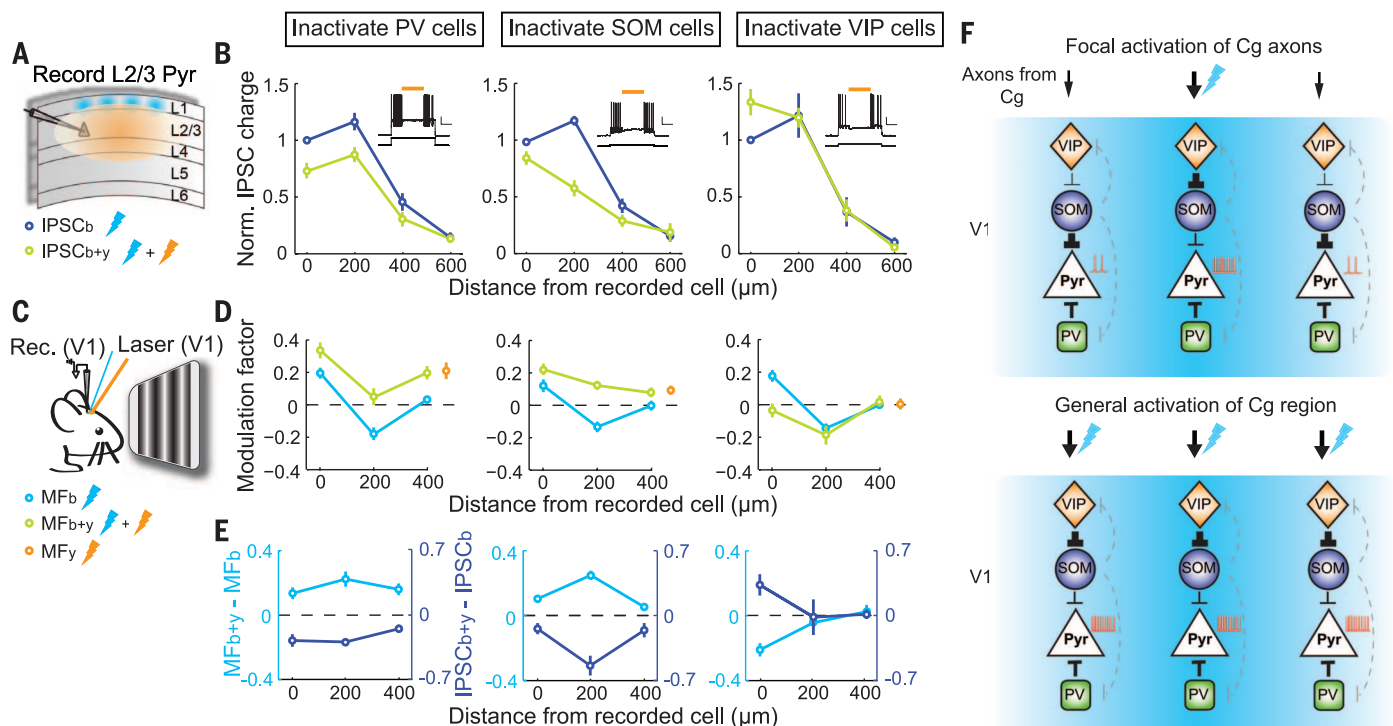


Fig. 4. Contributions of PV+, SOM+, and VIP+ neurons to disinaptic inhibition and top-down modulation. (A) Schematic of slice experiment. Thunderbolt denotes laser stimulation. (B) (Left) Normalized IPSC charge versus blue light location with (green) or without (blue) PV+ neuron inactivation. Reduction of IPSC was found at 0 μm ($P = 0.004$, $n = 9$ neurons), 200 μm and 400 μm ($P = 0.009$). (Insets) Yellow laser suppressed firing of depolarization-induced PV+ neuron firing (top, membrane potential; yellow bar, yellow laser duration; bottom, current injection; scale bars, 0.5 s, 20 mV/500 pA). (Middle and right) Inactivation of SOM+ ($n = 10$ neurons; 0 μm, $P = 0.04$; 200 μm, $P = 7 \times 10^{-4}$; 400 μm, $P = 0.04$) and VIP+ ($n = 9$ neurons; 0 μm, $P = 0.02$; 200 μm, $P = 0.92$; 400 μm, $P = 0.81$) neurons. Data were from more than three mice in each group. (C) Schematic of in vivo experiment. (D) Modulation

factor versus location of Cg axon stimulation with (green) or without (light blue) PV+, SOM+, or VIP+ neuron inactivation ($n \geq 16$ neurons for each point). PV+ inactivation, 0 μm, $P = 0.005$; 200 μm, $P = 6 \times 10^{-4}$; 400 μm, $P = 5 \times 10^{-4}$. SOM+ inactivation, 0 μm, $P = 2 \times 10^{-4}$; 200 μm, $P = 1 \times 10^{-8}$; 400 μm, $P = 0.02$. VIP+ inactivation, 0 μm, $P = 5 \times 10^{-5}$; 200 μm, $P = 0.34$; 400 μm, $P = 0.59$. Yellow circles indicate modulation factor with yellow light only. (E) Changes in modulation factor (light blue) and normalized IPSC charge (dark blue) induced with yellow light. (F) Diagrams of V1 circuits recruited by Cg projection. (Top) Focal activation. (Bottom) General activation. Thunderbolt denotes site of Cg axon activation. Black lines indicate connections important for top-down modulation; line width represents amplitude of synaptic input. Dashed gray lines indicate other known connections.

FEF (although the FEF projects primarily to higher visual areas rather than V1). In primate visual cortex, top-down attention enhances the firing rates of putative inhibitory interneurons (14, 36). In our study, the three subtypes of interneurons were all innervated by Cg, but they play different roles in top-down modulation. SOM+ neurons strongly inhibit pyramidal neurons in response to Cg input 200 μm away. That they also mediate suppression by visual stimuli outside of the receptive field (26) suggests that both bottom-up visual processing and top-down attentional modulation use a common mechanism for surround suppression (37). Disinhibition of pyramidal neurons by VIP+ neurons has also been shown in somatosensory (31), visual (33), auditory, and medial prefrontal (35) cortices, mediating firing rate increases induced by motor activity or reinforcement signals. In the top-down modulation studied here, the disinhibition is highly localized at the site of Cg axon activation (Fig. 4). On the basis of the effect of Halo-mediated inactivation of each cell type, we constructed a simple circuit diagram (Fig. 4F). The Cg→V1 projection provides direct inputs to both GABAergic and pyramidal

neurons. In response to focal Cg axon activation, SOM+ and PV+ neurons inhibit pyramidal neurons over a broad cortical area (with SOM+ neurons as a major source of inhibition at 200 μm), whereas VIP+ neurons selectively enhance the responses at 0 μm through localized inhibition of SOM+ neurons (Fig. 4F, left). In contrast, activation of the Cg region induced only facilitation and no suppression (Fig. 2). This may be because given the orientation and small size of Cg (Fig. 1B), topical laser stimulation inevitably activates a large proportion of V1-projecting neurons, causing broad activation of VIP+ neurons that overrides SOM-mediated surround inhibition (Fig. 4F, right). On the other hand, dual retrograde tracing suggests that individual Cg neurons project to restricted regions of V1 (fig. S8), allowing spatially specific top-down modulation.

In addition to PV+, SOM+, and VIP+ neurons, layer 1 GABAergic neurons may also receive Cg innervation, providing both inhibition and disinhibition to pyramidal neurons (38, 39). Besides Cg projection to layer 1, other pathways may also contribute to top-down modulation, including the projection to V1 layer 6 and indirect path-

ways through other brain areas (16–19, 40). Furthermore, whereas spatial attention involves center-surround modulation in the space domain, feature attention also biases the competition between attended and unattended stimuli (7), perhaps via circuit mechanisms similar to those described here but operating in higher visual areas in stimulus feature space (41). Enhancing neuronal representation of relevant input and filtering out irrelevant stimuli are two equally important aspects of selective attention. Long-range glutamatergic projections can exert both types of modulation by activating local circuits that contain distinct subtypes of GABAergic interneurons.

REFERENCES AND NOTES

1. R. Desimone, J. Duncan, *Annu. Rev. Neurosci.* **18**, 193–222 (1995).
2. S. Kastner, L. G. Ungerleider, *Annu. Rev. Neurosci.* **23**, 315–341 (2000).
3. J. H. Reynolds, D. J. Heeger, *Neuron* **61**, 168–185 (2009).
4. S. Treue, J. H. Maunsell, *J. Neurosci.* **19**, 7591–7602 (1999).
5. J. W. Bisley, M. E. Goldberg, *Annu. Rev. Neurosci.* **33**, 1–21 (2010).
6. E. K. Miller, J. D. Cohen, *Annu. Rev. Neurosci.* **24**, 167–202 (2001).
7. R. F. Squire, B. Noudoost, R. J. Schaffer, T. Moore, *Annu. Rev. Neurosci.* **36**, 451–466 (2013).
8. H. Zhou, R. Desimone, *Neuron* **70**, 1205–1217 (2011).

OCEANOGRAPHY

Centennial changes in North Pacific anoxia linked to tropical trade winds

Curtis Deutsch,^{1*} William Berelson,² Robert Thunell,³ Thomas Weber,¹ Caitlin Tems,² James McManus,^{4†} John Crusius,⁵ Taka Ito,⁶ Timothy Baumgartner,⁷ Vicente Ferreira,⁷ Jacob Mey,^{8,9} Alexander van Geen⁸

Climate warming is expected to reduce oxygen (O₂) supply to the ocean and expand its oxygen minimum zones (OMZs). We reconstructed variations in the extent of North Pacific anoxia since 1850 using a geochemical proxy for denitrification ($\delta^{15}\text{N}$) from multiple sediment cores. Increasing $\delta^{15}\text{N}$ since ~1990 records an expansion of anoxia, consistent with observed O₂ trends. However, this was preceded by a longer declining $\delta^{15}\text{N}$ trend that implies that the anoxic zone was shrinking for most of the 20th century. Both periods can be explained by changes in winds over the tropical Pacific that drive upwelling, biological productivity, and O₂ demand within the OMZ. If equatorial Pacific winds resume their predicted weakening trend, the ocean's largest anoxic zone will contract despite a global O₂ decline.

Below the ocean's surface, the decomposition of sinking detritus creates a layer of low-O₂ water inhospitable to many marine species (1). These oxygen minimum zones (OMZs) are predicted to expand with climate warming (2, 3), causing a major disruption to ecosystems, especially in areas where OMZ waters impinge on coastal environments already under low-O₂ stress from natural or human causes (4–6). This putative expansion stems from two direct consequences of climate change: As the surface ocean warms, its gas solubility and density both decrease, reducing the concentration of O₂ in surface water and the rate at which that water is transported downward against a more stable stratification. The resulting decline in O₂ supply to the ocean interior is generally supported by observed trends toward lower O₂ over the past few decades, over many parts of the world's oceans (7), including the strong OMZs in the tropics (8).

The climatic response of the OMZ also depends on O₂ demand, although the factors governing those biological rates are less well understood. Earth system model simulations project large future decreases in the sinking flux of organic matter throughout the tropics (9), which should reduce O₂ demand in the OMZ, counteracting

the loss of O₂ supply. In the eastern tropical and subtropical Pacific Ocean, the OMZ variability over the last 50 years appears to have been driven primarily by O₂ demand, which is strongly modulated by decadal climate variability (10, 11). In light of that variability, the instrumental O₂ record is still sparse and short, making long-term trends in the OMZ difficult to detect or attribute especially in the most intense tropical OMZs in the Pacific and Indian oceans (8, 12). The relative strength of future changes in O₂ supply versus demand in the tropical OMZ would be clearer if their long-term response to the climate warming since the industrial revolution were known.

We reconstructed changes in the OMZ of the eastern tropical northern Pacific (ETNP) over the past 150 years using a geochemical proxy for water column anoxia that is recorded in sediments (Fig. 1). At the eastern terminus of the OMZ, where thermocline waters shoal toward the productive surface layer, respiration depletes O₂ and anaerobic bacteria begin reducing nitrate (NO₃[−]) to oxidize organic matter (13) (Fig. 1). This denitrification process preferentially removes the lighter ¹⁴N isotope of N, leaving a residual NO₃[−] pool enriched in heavier ¹⁵N (14, 15). The resulting nitrate with a high isotope ratio, $\delta^{15}\text{N} = ((^{15}\text{N}/^{14}\text{N})/R_{\text{air}} - 1) \times 1000$, where R_{air} is the N isotope ratio in air, is upwelled to the surface, where it can be transferred to plankton communities and then, via sinking particles, into sediments (16, 17). In regions with complete consumption of upwelled nitrate, the $\delta^{15}\text{N}$ of particulate organic nitrogen (PON) accumulating on the sea floor closely resembles that of nitrate in waters at ~100 m (18). In the absence of postdepositional alteration, downcore variations in $\delta^{15}\text{N}$ provide a history of the integrated rates of denitrification and the size of the OMZ to which it is confined (19, 20).

To ensure a representative history of changes in OMZ intensity, we analyzed sediment cores from three sites along the North American margin

9. T. J. Buschman, E. K. Miller, *Science* **315**, 1860–1862 (2007).
10. G. G. Gregoriou, S. J. Gotts, H. Zhou, R. Desimone, *Science* **324**, 1207–1210 (2009).
11. T. Moore, K. M. Armstrong, *Nature* **421**, 370–373 (2003).
12. B. Noudoost, T. Moore, *Nature* **474**, 372–375 (2011).
13. L. B. Ekstrom, P. R. Roelfsema, J. T. Arsenault, G. Bonmassar, W. Vanduffel, *Science* **321**, 414–417 (2008).
14. Y. Chen et al., *Nat. Neurosci.* **11**, 974–982 (2008).
15. K. A. Sundberg, J. F. Mitchell, J. H. Reynolds, *Neuron* **61**, 952–963 (2009).
16. K. McAlonan, J. Cavanaugh, R. H. Wurtz, *Nature* **456**, 391–394 (2008).
17. G. Purushothaman, R. Marion, K. Li, V. A. Casagrande, *Nat. Neurosci.* **15**, 905–912 (2012).
18. M. Sarter, M. E. Hasselmo, J. P. Bruno, B. Givens, *Brain Res. Brain Res. Rev.* **48**, 98–111 (2005).
19. Y. B. Saalman, M. A. Pinsky, L. Wang, X. Li, S. Kastner, *Science* **337**, 753–756 (2012).
20. M. A. Segraves, M. E. Goldberg, *J. Neurophysiol.* **58**, 1387–1419 (1987).
21. The projection to superior colliculus arises only from deep layers (Fig. 1D), similar to that in primate FEF.
22. S. True, J. C. Martínez Trujillo, *Nature* **399**, 575–579 (1999).
23. T. Moore, M. Fallah, *J. Neurophysiol.* **91**, 152–162 (2004).
24. X. Xu, K. D. Roby, E. M. Callaway, *J. Comp. Neurol.* **518**, 389–404 (2010).
25. G. Fishell, B. Rudy, *Annu. Rev. Neurosci.* **34**, 535–567 (2011).
26. H. Adesnik, W. Bruns, H. Taniguchi, Z. J. Huang, M. Scanziani, *Nature* **490**, 226–231 (2012).
27. S. H. Lee et al., *Nature* **488**, 379–383 (2012).
28. N. R. Wilson, C. A. Runyan, F. L. Wang, M. Sur, *Nature* **488**, 343–348 (2012).
29. L. Petreanu, T. Mao, S. M. Sternson, K. Svoboda, *Nature* **457**, 1142–1145 (2009).
30. I. R. Wickersham et al., *Neuron* **53**, 639–647 (2007).
31. S. Lee, I. Kruglikov, Z. J. Huang, G. Fishell, B. Rudy, *Nat. Neurosci.* **16**, 1662–1670 (2013).
32. L. Madisen et al., *Nat. Neurosci.* **15**, 793–802 (2012).
33. Y. Fu et al., *Cell* **156**, 1139–1152 (2014).
34. C. K. Pfeffer, M. Xue, M. He, Z. J. Huang, M. Scanziani, *Nat. Neurosci.* **16**, 1068–1076 (2013).
35. H. Lee, I. Kruglikov, Z. J. Huang, G. Fishell, B. Rudy, *Nat. Neurosci.* **16**, 1139–1152 (2013).
36. J. F. Mitchell, K. A. Sundberg, J. H. Reynolds, *Neuron* **55**, 131–141 (2007).
37. Based on a magnification factor of 10 μm per degree in mouse V1 (42), 200 μm of cortical distance corresponds to 20° of visual angle. A previous study (26) showed that for most neurons, the preferred size of visual stimulus was <15° in radius, and stimuli beyond this radius suppressed neuronal responses. This suggests that surround suppression for top-down modulation and bottom-up processing occur on similar spatial scales. The same inhibitory circuits could also contribute to decreased receptive field similarity and signal correlation between V1 neurons over ~200 μm (42).
38. J. J. Letzkus et al., *Nature* **480**, 331–335 (2011).
39. X. Jiang, G. Wang, A. J. Lee, R. L. Stornetta, J. J. Zhu, *Nat. Neurosci.* **16**, 210–218 (2013).
40. S. P. Mysore, E. I. Knudsen, *Nat. Neurosci.* **16**, 473–478 (2013).
41. S. Ardid, X. J. Wang, A. Compte, *J. Neurosci.* **27**, 8486–8495 (2007).
42. V. Bonin, M. H. Histed, S. Yurgenson, R. Clay Reid, *J. Neurosci.* **31**, 18506 (2011).

ACKNOWLEDGMENTS

We thank L. Pinto and Y. Zhu for help with data analysis; S. H. Lee and M. Zhao for technical assistance; Standford Neuroscience Gene Vector and Virus Core for AAV-DJ supply; K. Deisseroth, E. Callaway, B. Lim, and B. C. Weissbourd for virus and constructs; and R. Desimone, L. Wang, and M. A. Segraves for helpful discussions. This work was supported by NIH grant R01 EY018861, NSF grant 22250400-42533, a Uehara Memorial Foundation fellowship, and the Human Frontier Science Program. All primary histological, electrophysiological, and behavioral data are archived in the Department of Molecular and Cell Biology, University of California, Berkeley.

SUPPLEMENTARY MATERIALS

www.sciencemag.org/content/345/6197/660/suppl/DC1
Materials and Methods
Figs. S1 to S8
References (43–51)

31 March 2014; accepted 27 June 2014
10.1126/science.1254126

¹School of Oceanography, University of Washington, Seattle, WA, USA. ²Department of Earth Sciences, University of Southern California, Los Angeles, CA, USA. ³Department of Earth and Ocean Sciences, University of South Carolina, Columbia, SC, USA. ⁴College of Earth, Ocean, and Atmospheric Sciences, Oregon State University, Corvallis, OR, USA. ⁵U.S. Geological Survey, University of Washington School of Oceanography, Seattle, WA, USA. ⁶School of Earth and Atmospheric Sciences, Georgia Institute of Technology, Atlanta, GA, USA. ⁷Departamento de Oceanografía Biológica, Centro de Investigación Científica y de Educación Superior de Ensenada, Baja California, México. ⁸Lamont-Doherty Earth Observatory of Columbia University, Palisades, NY, USA. ⁹Department of Physical Sciences, Kingsborough Community College, City University of New York, New York, NY, USA.
*Corresponding author. E-mail: cdeutsch@uw.edu †Present address: Department of Geosciences, University of Akron, Akron, OH, USA.